

Mechanism of Li₂S formation and dissolution in Lithium-Sulphur batteries

Christian Prehal (✉ cprehal@ethz.ch)

ETH Zurich

Sara Drvarič Talian

National Institute of Chemistry <https://orcid.org/0000-0003-1355-2843>

Alen Vizintin

National Institute of Chemistry <https://orcid.org/0000-0003-1876-1396>

Heinz Amenitsch

Graz University of Technology

Robert Dominko

National Institute of Chemistry <https://orcid.org/0000-0002-6673-4459>

Stefan Freunberger

Institute of Science and Technology Austria <https://orcid.org/0000-0003-2902-5319>

Vanessa Wood

Swiss Federal Institute of Technology in Zurich <https://orcid.org/0000-0001-6435-0227>

Article

Keywords: Li₂S, Lithium Sulphur Batteries, SAXS, WAXS

Posted Date: August 16th, 2021

DOI: <https://doi.org/10.21203/rs.3.rs-818607/v1>

License:  This work is licensed under a Creative Commons Attribution 4.0 International License.

[Read Full License](#)

Mechanism of Li₂S formation and dissolution in Lithium-Sulphur batteries

Christian Prehal^{1,*}, Sara Drvarič Talian², Alen Vizintin², Heinz Amenitsch⁴, Robert Dominko^{2,3}, Stefan A. Freunberger^{5,*}, Vanessa Wood^{1,*}

1. Department of Information Technology and Electrical Engineering, ETH Zürich, Gloriastrasse 35, 8092 Zürich, Switzerland

2. Department of Materials Chemistry, National Institute of Chemistry, Hajdrihova 19, 1000 Ljubljana, Slovenia

3. Faculty of Chemistry and Chemical Technology University of Ljubljana, Večna pot 113, 1000 Ljubljana, Slovenia

4. Institute for Inorganic Chemistry, Graz University of Technology, Stremayrgasse 9, 8010 Graz, Austria

5. IST Austria (Institute of Science and Technology Austria), Am Campus 1, 3400 Klosterneuburg, Austria

* Corresponding authors' e-mail: cprehal@ethz.ch, stefan.freunberger@ist.ac.at, vwood@ethz.ch

Abstract

Insufficient understanding of the mechanism that reversibly converts sulphur into lithium sulphide (Li₂S) via soluble polysulphides (PS) hampers the realization of high performance lithium-sulphur cells. Typically Li₂S formation is explained by direct electroreduction of a PS to Li₂S; however, this is not consistent with the size of the insulating Li₂S deposits. Here, we use in situ small and wide angle X-ray scattering (SAXS/WAXS) to track the growth and dissolution of crystalline and amorphous deposits from atomic to sub-micron scales during charge and discharge. Stochastic modelling based on the SAXS data allows quantification of the chemical phase evolution during discharge and charge. We show that Li₂S deposits predominantly via disproportionation of transient, solid Li₂S₂ to form primary Li₂S crystallites and solid Li₂S₄ particles. We further demonstrate that this process happens in reverse during charge. These findings show that the discharge capacity and rate capability in Li-S battery cathodes are therefore limited by mass transport through the increasingly tortuous network of Li₂S / Li₂S₄ / carbon pores rather than electron transport through a passivating surface film.

1 Main

2 Lithium-sulphur (Li-S) batteries are considered strategic candidates to reduce the environmental impact of
3 current Li-ion batteries¹. The high expectations arise from the large theoretical capacities, abundance, and
4 low cost of sulphur²⁻⁴. Li-S batteries reversibly cycle sulfur to lithium sulfide (S / Li₂S), typically in a highly
5 porous carbon cathode soaked with a liquid, non-aqueous electrolyte and using a lithium metal anode.
6 Discharge converts S to Li₂S stepwise via polysulfides (PSs) Li₂S_x (2 < x < 8). Practical realization of Li-S
7 cells is hindered by incomplete S utilization, poor S/Li₂S mass loadings, rapid capacity fading, low rate
8 capabilities, and irreversible reactions of PSs at the anode^{3,5,6}. These issues all trace back to insufficient
9 understanding of S-to-Li₂S conversion.

10 The physical-chemical mechanism to reversibly form and dissolve solid Li₂S remains controversial^{7,8}. Many
11 studies consider Li₂S to form via direct electroreduction of Li₂S₂ (or higher-order PSs) at the carbon-electrolyte
12 interface⁸⁻¹². However, as electrodeposition of an insulator is in principle self-limited, the fact that Li₂S deposits
13 are beyond tens and hundreds of nm in size¹³⁻¹⁵ suggest that they form via a solution-mediated process. This
14 is supported by the finding that capacity is limited by mass transport in the tortuous Li₂S-carbon pore
15 network.¹⁶⁻¹⁸ Such a solution-mediated processes could be the direct electroreduction of molecular Li₂S₂ to
16 dissolved Li₂S (2 Li⁺, S²⁻), which then precipitates solid Li₂S crystallites, similar to the electrodeposition of
17 NaO₂ or KO₂ in Na-O₂ and K-O₂ batteries¹⁹. However, large deposits beyond tens or hundreds of nanometers
18 would require a solubility of Li₂S beyond the reported 10⁻⁶ M¹⁵. Disproportionation of PSs is widely accepted,⁷
19 and some studies consider Li₂S to form via disproportionation of dissolved Li₂S₄^{13,16,20}.

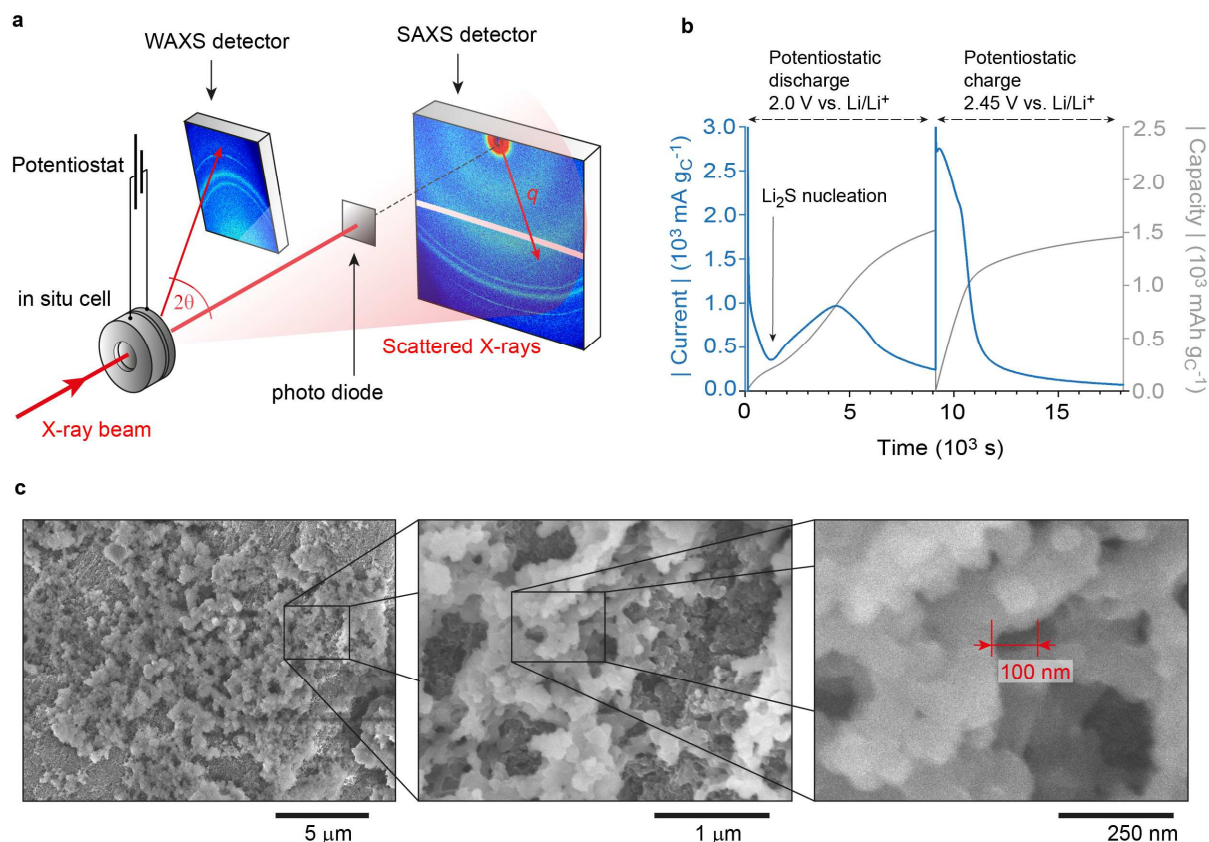
20 While *operando* x-ray diffraction^{21,22} and spectroscopy²³⁻²⁶ provide insights into the chemistries occurring
21 during (de)lithiation, a complete understanding of the mechanisms of Li₂S formation requires a detailed
22 chemical as well as structural picture. While the structures within Li-S has been studied using (*operando*)
23 electron and X-ray microscopy²⁷⁻³⁰, these techniques are limited by impractical cell designs, the Li₂S stability,
24 the resolution, field of view, and the challenges of 3D imaging. Small angle scattering can provide
25 complementary structural sensitivity from sub-nm to 100 nm, regardless of whether the probed phases are
26 crystalline, amorphous or liquid³¹. A recent *operando* small angle neutron scattering study confirmed the
27 ability to follow the evolution of Li₂S particles not much larger than a few nm³². Neutron and x-ray scattering
28 are complementary methods since the phases are probed with different scattering contrasts.

29 Here, we perform *in situ* small and wide-angle X-ray scattering (SAXS/WAXS) to gain simultaneous structural
30 and chemical insights from atomic to sub-micrometer scales with time resolutions of several seconds.³³⁻³⁵
31 Stochastic modelling enables quantitative interpretation of the SAXS results.^{28, 41} During lithiation, we observe
32 the formation of a hierarchical structure, consisting of aggregates of Li₂S crystallites and a second solid phase,
33 which we identify to be Li₂S₄, both of which formed by disproportionation of the short chain PS Li₂S₂. During
34 delithiation, the reverse occurs with the dissolution of the Li₂S / Li₂S₄ composite nanostructure via
35 comproportionation to a Li₂S₂ polysulfide in solution. Complementary information from x-ray diffraction,
36 electron microscopy, and electrochemical measurements allows us to validate this model for (de)lithiation.
37 These findings show that discharge capacities and rates in Li-S batteries are limited by mass transport of PSs
38 through the tortuous solid deposits and give insights into how cells design, electrolyte selection, and cycling
39 proposals that control the Li₂S morphology can be used to optimize performance.¹⁷

40 ***In situ* small and wide angle X-ray scattering**

41 *In situ* SAXS/WAXS experiments are carried out with a commercial electrochemical *in situ* scattering cell³³
42 holding a high surface area carbon black cathode, a Li metal anode and a catholyte comprising 0.5 M Li₂S₈,
43 1 M LiTFSI, and 0.4 M LiNO₃ in diethylene glycol dimethyl ether (2G). To verify that our findings hold more
44 generally, we also perform *in situ* SAXS/WAXS experiments on another common system with a carbon black
45 / sulphur composite cathode and 1 M LiTFSI in tetraethylene glycol dimethyl ether:dioxolane (TEGDME:DOL,
46 1:1) without PSs as the electrolyte (Supplementary Fig. 1). SAXS and WAXS intensities are recorded on
47 separate areal detectors (Fig. 1a) with a time resolution of 1 min during potentiostatic discharge/charge. The

1 x-ray beam hit the Li metal anode, the catholyte soaked separator and the carbon black cathode. All reversible
 2 structural changes seen by *in situ* SAXS/WAXS stem from the reversible deposition / dissolution of active
 3 material in the carbon black cathode only (Supplementary Fig. 2). More details are given in the Methods.



4
 5 **Figure 1 | *In situ* SAXS / WAXS experimental set-up and potentiostatic discharge / charge.** a, Sketch of the
 6 experimental set-up for *in situ* SAXS / WAXS experiments at ELETTRA³⁶ showing the separate detectors. b, Absolute
 7 specific current (blue) and absolute specific capacity (grey) versus time during potentiostatic discharge / charge of the *in situ*
 8 SAXS cell at 2.0 V / 2.45 V vs. Li/Li⁺. Both current and capacity are normalized by the bare carbon black electrode
 9 mass. c, Scanning electron microscopy images at different magnification show the hierarchical structure of Li_2S deposits
 10 on the carbon black electrode after potentiostatic discharge at 2.0 V vs. Li/Li⁺ to a capacity of 1520 mAh gC^{-1} .

11 The (dis)charge profile in the *in situ* cell shows the expected behavior of a Li-S system (Fig. 1b). The absolute
 12 current during potentiostatic discharge at 2.0 V vs. Li/Li⁺ exhibits a distinct minimum indicating the onset of
 13 Li_2S nucleation. After nucleation, the current (i.e., the Li_2S formation rate) increases, since growth of Li_2S on
 14 existing Li_2S nuclei occurs at a lower activation energy than initial nucleation. The reduction in current after
 15 ~ 4500 s indicates the onset of capacity-limiting processes. The discharge is stopped after 2.5 h at a capacity
 16 of 1520 mAh gC^{-1} (normalized by the carbon mass, as there is no defined amount of sulphur present at the
 17 cathode). The maximum theoretical capacity of Li_2S_8 in the 60 μl catholyte corresponds to ca. 2000 mAh gC^{-1} ,
 18 which is larger than the maximum values in Fig. 1b. Consistent with literature^{15,16}, SEM images of electrodes
 19 after full potentiostatic discharge show large structures with particle sizes beyond 100 nm (Fig. 1c) Due to the
 20 poor electronic conductivity of Li_2S , the resolution of SEM is not sufficient to resolve the nanostructure below
 21 100 nm properly; however, these insights can be obtained by SAXS. During charge at 2.45 V vs. Li/Li⁺ for the
 22 same time, initially high currents fade quickly after $\sim 2/3$ of the capacity.

23 The initial SAXS intensity prior to discharge shows a roughly linear decay in the double-logarithmic plot
 24 (Fig. 2a). Such power law behavior is typical for the fractal-like structure of carbon black electrodes. During
 25 discharge, the SAXS intensity generally increases, with a larger increase at high q around 1.5 nm^{-1} and at

1 low q around 0.2 nm^{-1} . The background-corrected WAXS intensities indicate the formation of Li_2S crystallites
2 during discharge (Fig. 2b).

3 To visualize the subtle SAXS intensity changes during the full potentiostatic discharge / charge cycle, we plot
4 the relative SAXS intensity change with respect to the initial SAXS intensity prior to discharge as a function
5 of time and scattering vector length q (Fig. 2c, d). The WAXS intensity is also plotted as a function of time
6 and scattering angle in Fig. 2e. As solid Li_2S starts to form (as evidenced by the decreasing current at ~ 5000
7 s in Fig. 2c and the emergence of the Li_2S crystallites in Fig. 2e), two distinct SAXS intensity maxima appear
8 at low q (regime q_A) and at high q (regime q_B). In line with the high currents during charge (Fig. 1b, 2c), these
9 features disappear quickly during charge compared to their emergence during discharge.

10 Comparing the changes in intensities of the SAXS and WAXS features (Fig. 2f) shows similarities in
11 emergence of the WAXS and the high q SAXS feature during discharge. Meanwhile the low q SAXS feature
12 decreases at the end of discharge. During charge, the low q SAXS feature decreases quickest. The WAXS
13 signal from the Li_2S crystallites decreases slower, with the high q feature decreasing even slower. These
14 observations suggest that the SAXS intensity maxima, while related to Li_2S deposition and dissolution, do not
15 correlate directly to the Li_2S crystallites probed by WAXS.

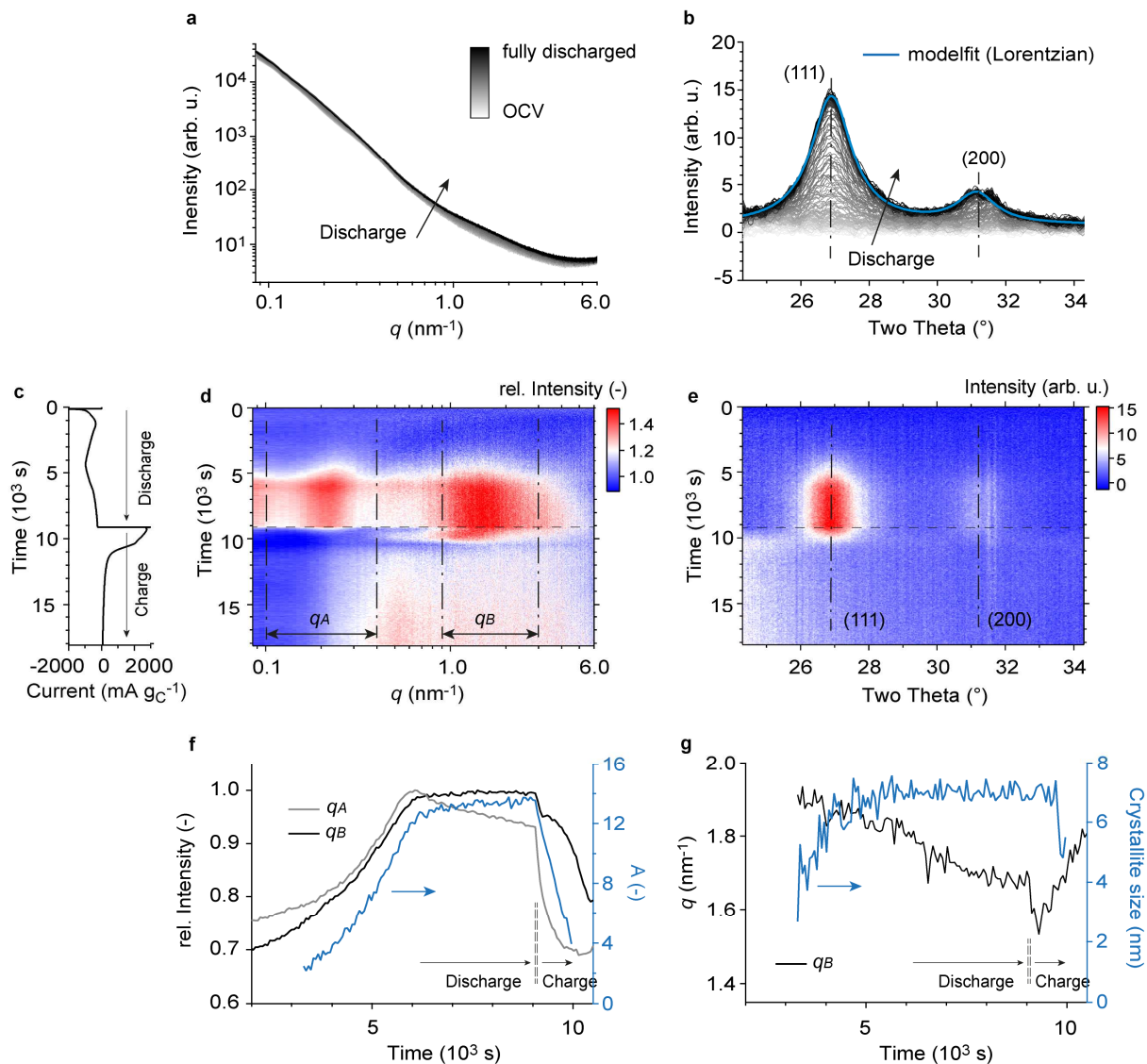
16 This suggestion is further supported when considering the sizes of the features. From WAXS, we use the
17 Scherrer equation to estimate that the Li_2S crystallite size (i.e., mean diameter) increases and plateaus at
18 about $\sim 7 \text{ nm}$ (Fig. 2g). Spherical 7 nm single crystal particles should in a first approximation cause a broad
19 SAXS intensity peak around 0.6 nm^{-1} (Supplementary Fig. 3). However, neither the high- q (1.5 nm^{-1}) nor the
20 low- q (0.2 nm^{-1}) SAXS intensity maximum relates to this primary Li_2S crystallite size, instead indicating
21 features of approximately 2.5 nm and 24 nm , respectively.

22 To verify whether the features seen in the SAXS / WAXS data are specific to our selected materials and
23 operating conditions, we galvanostatically discharge a sulphur / carbon black electrode (ENSACO 350G,
24 Imerys) in a $1 \text{ M LiTFSI} / \text{TEGDME:DOL}$ (1:1 vol.%) electrolyte at three different currents (Supplementary
25 Fig. 1). For all currents, we find a $6 - 7 \text{ nm}$ Li_2S crystallite size from the WAXS diffraction peak fitting and a
26 high q SAXS intensity maximum between $1 - 2 \text{ nm}^{-1}$. Primary Li_2S crystallite formation can therefore not be
27 explained by classical nucleation and continuous growth^{37,38}, which would result in a crystallite size that
28 strongly depends on current.

29 On the other hand, the low q intensity maximum depends on the applied current (Supplementary Fig. 1). With
30 increasing current, the intensity shifts to higher q -values (from $\sim 0.1 \text{ nm}^{-1}$ at $C/3$ to $\ll 0.08 \text{ nm}^{-1}$ at $C/30$). We
31 therefore attribute our low q feature to aggregates comprised of the smaller primary Li_2S crystallites. At higher
32 current, we have more, smaller aggregates which is in principle consistent with heterogenous nucleation and
33 growth³⁹.

34 These SAXS/WAXS findings are in line with previous experimental data. Independently of the used materials
35 or applied current^{13,15,16,22,39}, the Li_2S primary crystallite size has been shown to remain around 10 nm . Size
36 and shape of the super-structures on the other hand, are very sensitive to the used materials and conditions
37 such as current density^{11,15,16,39}. A feature similar to our signal at low- q was observed using small angle
38 neutron scattering³². Finally, the Li_2S deposits observed with SEM are known to be larger than the primary
39 crystallite size estimated by XRD via the Scherrer equation^{15,16}.

40 New in this work is the high- q SAXS intensity maximum corresponding to a feature with $\sim 2.5 \text{ nm}$ diameter.
41 Understanding the origin of this feature can provide the missing piece of the puzzle in quantifying Li_2S
42 formation and dissolution.



1
2 **Figure 2 | In situ SAXS/WAXS experimental data.** **a**, SAXS intensities versus scattering vector length q during
3 potentiostatic discharge at 2.0 V vs. Li/Li^+ up to a capacity of 1520 $\text{mAh g}_\text{C}^{-1}$. **b**, The respective background corrected
4 WAXS intensities versus scattering angle during potentiostatic discharge. The (111) and (200) Li_2S diffraction peaks are
5 fitted using a Lorentz function. **c**, Specific current versus time during potentiostatic discharge / charge at 2.0 V / 2.45 V vs.
6 Li/Li^+ . **d**, The relative SAXS intensity change as a function time and the scattering vector length q . The SAXS intensities
7 were normalized by the SAXS intensity prior to discharge at OCV. The q -regions q_A and q_B embrace intensity maxima that
8 appear upon Li_2S formation at low and high q , respectively. **e**, The WAXS intensities as a function of time and scattering
9 angle. The dash-dotted lines indicate the (111) and (200) Li_2S diffraction peaks. **f**, Normalized, mean SAXS intensity of
10 the low- q (q_A) and high- q (q_B) regimes during potentiostatic discharge / charge (black and grey) and (111) diffraction peak
11 height A in blue (obtained from Lorentzian peak fit). **g**, Shift of the SAXS intensity maximum in q_B , obtained by calculating
12 the “center of mass” in the q_B regime (black) and Li_2S crystallite size in blue (obtained from the (111) peak width and the
13 Scherrer equation) during potentiostatic discharge / charge.

14 Li_2S formation via polysulfide disproportionation

15 To develop a model for the chemical phase evolution and observed hierarchical structures that can be
16 validated with the SAXS data, we consider potential scenarios for Li_2S formation. The observed aggregate
17 sizes of more than 100 nm combined with the insulating nature of Li_2S mean that is highly improbable that
18 Li_2S forms via direct electroreduction and growth at the carbon/electrolyte interface or Li_2S /electrolyte
19 interface³⁴. Instead, the structural features point to species in the electrolyte supporting growth. This could be
20 Li_2S if it redissolves (Li^+ , S^{2-}) and precipitates after having formed by direct reduction at the carbon; however,

1 the extremely low solubility of Li_2S^{15} suggests that dissolved Li^+ and S_2^- could only form small Li_2S crystallites
 2 on or in close proximity to the carbon surface. Alternatively, it could be solution transport of PSs, which after
 3 diffusing in solution to a nucleation site disproportionate to form Li_2S (for example, $\text{Li}_2\text{S}_2 \rightarrow 2/3 \text{Li}_2\text{S} + 1/3$
 4 Li_2S_4) (Fig. 3a).

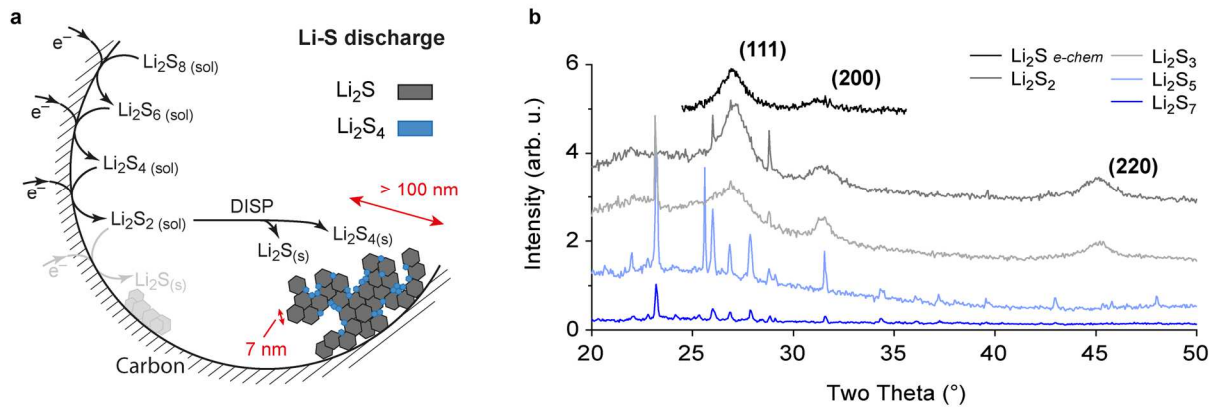
5 If Li_2S forms via disproportionation of PSs, we also expect PSs synthesized via chemical routes to
 6 disproportionate to Li_2S and a higher-order PS. To test this, we prepare solid PSs from their solutions and
 7 investigate whether Li_2S forms. We mix sulphur and Li metal in a solution of tetrahydrofuran (THF) at 50 °C
 8 to obtain nominal stoichiometries of Li_2S_2 , Li_2S_3 , Li_2S_5 and Li_2S_7 . The stirring time to completely dissolve all S
 9 and Li varies between 1 day for nominally Li_2S_7 to 2 weeks for Li_2S_2 . The solutions are dried under vacuum
 10 to obtain solid PS powders (details in the Methods).

11 X-ray diffraction patterns of the resulting solid PSs (Fig. 3b) show that the low-order PSs (nominal
 12 stoichiometry Li_2S_2 and Li_2S_3) contain crystalline Li_2S . Sharp diffraction peaks in the higher-order PSs indicate
 13 larger sulphur (α -S) crystallites. Ex situ nuclear magnetic resonance (NMR) spectra of PS powders confirm
 14 the coexistence of Li_2S and other higher order PS (or S)⁴⁰. Interestingly, SAXS intensities of the nominally
 15 Li_2S_2 and Li_2S_3 solids (Supplementary Fig. 4) reveal a high- q SAXS intensity shoulder as observed for the
 16 electrochemically discharged electrode (Fig. 2d and Fig. 4a). The Li_2S diffraction peak width of the Li_2S_2
 17 powder is nearly identical to the peak width of Li_2S obtained from electrochemical discharge, resulting in
 18 crystallite size of 5–7 nm. This indicates that Li_2S forms both in the electrochemical cell and upon drying PS
 19 solutions via disproportionation from solution species.

20 The fact that only low order PSs show crystalline Li_2S implies that the disproportionation educt is either Li_2S_2
 21 or Li_2S_3 . Since the latter is typically absent in glyme-based electrolytes,²⁰ we hypothesize that Li_2S forms and
 22 dissolves predominantly via



23 and that the high- q SAXS intensity maximum therefore stems from solid Li_2S_4 particles.



24
 25 **Figure 3 | Polysulfide disproportionation from solution.** **a**, Scheme of proposed reaction pathway during Li-S battery
 26 discharge. Solution-mediated disproportionation forms a solid Li_2S / Li_2S_4 composite. **b**, X-ray diffraction patterns (intensity
 27 vs. scattering angle Two Theta) of different solid polysulfides (nominally Li_2S_2 to Li_2S_7) as well as of the discharged
 28 electrode shown in Fig. 2b (Li_2S e-chem). The (111), (200), and (220) Li_2S diffraction peaks indicate Li_2S crystallites of
 29 similar size to form in Li_2S_2 , Li_2S_3 and Li_2S as well in upon electrochemical reduction (crystallite sizes: $\text{Li}_2\text{S}_2 = 5.7$ nm; Li_2S_3
 30 $= 3.4$ nm; obtained from the (111) diffraction peak and the Scherrer formula).

31 Formation of Li_2S via disproportionation of Li_2S_2 is consistent with a number of recent investigations, which
 32 predict the instability of Li_2S_2 ^{41,42}. Furthermore, as a sanity check that Li_2S_2 disproportionates to Li_2S and
 33 Li_2S_4 , we perform a simple experiment. Higher order polysulfides are soluble in glymes⁴³ so washing a dried,
 34 discharged electrode with fresh 2G should dissolve most Li_2S_4 . Indeed, ex-situ SAXS of the dried electrode

1 shows a pronounced high- q SAXS intensity shoulder that disappears after washing (Supplementary Fig. 2).
2 Alternative but unlikely SAXS data interpretations are discussed in Supplementary Note 1.

3 **A model for Li₂S Deposition and Dissolution**

4 Our experiments point to the following process for the formation and dissolution of Li₂S: during discharge,
5 solid Li₂S₂ precipitates and disproportionates, forming a composite structure consisting of solid Li₂S and Li₂S₄
6 particles (Fig. 3a). The solid Li₂S₄ particles are responsible for the SAXS feature in region q_B in Fig. 2d and
7 have a mean size around 2.5 nm. The 7 nm Li₂S crystallites (WAXS) and these Li₂S₄ particles aggregate to
8 form features with a mean size (diameter) around 24 nm (region q_A SAXS). These polycrystalline aggregates
9 arrange into the larger structures >100 nm seen by SEM (Fig. 1c). During charge, the aggregates first dissolve
10 into primary Li₂S and Li₂S₄ particles. Li₂S₄ dissolution lagging behind Li₂S dissolution during the entire charge
11 (in Fig 2f, the low- q maximum disappears faster than WAXS diffraction peaks and high- q shoulder).

12 To validate this and gain further insights into the structural evolution of the Li₂S/Li₂S₄ nanostructure, we use
13 the concept of plurigaussian random fields^{33,44} to create the three-phase Li₂S / Li₂S₄ / electrolyte structure
14 (Methods). With this structure, we then model the expected time-dependent SAXS intensity change during
15 discharge and charge based on our proposed mechanism and compare it to the measured SAXS data.

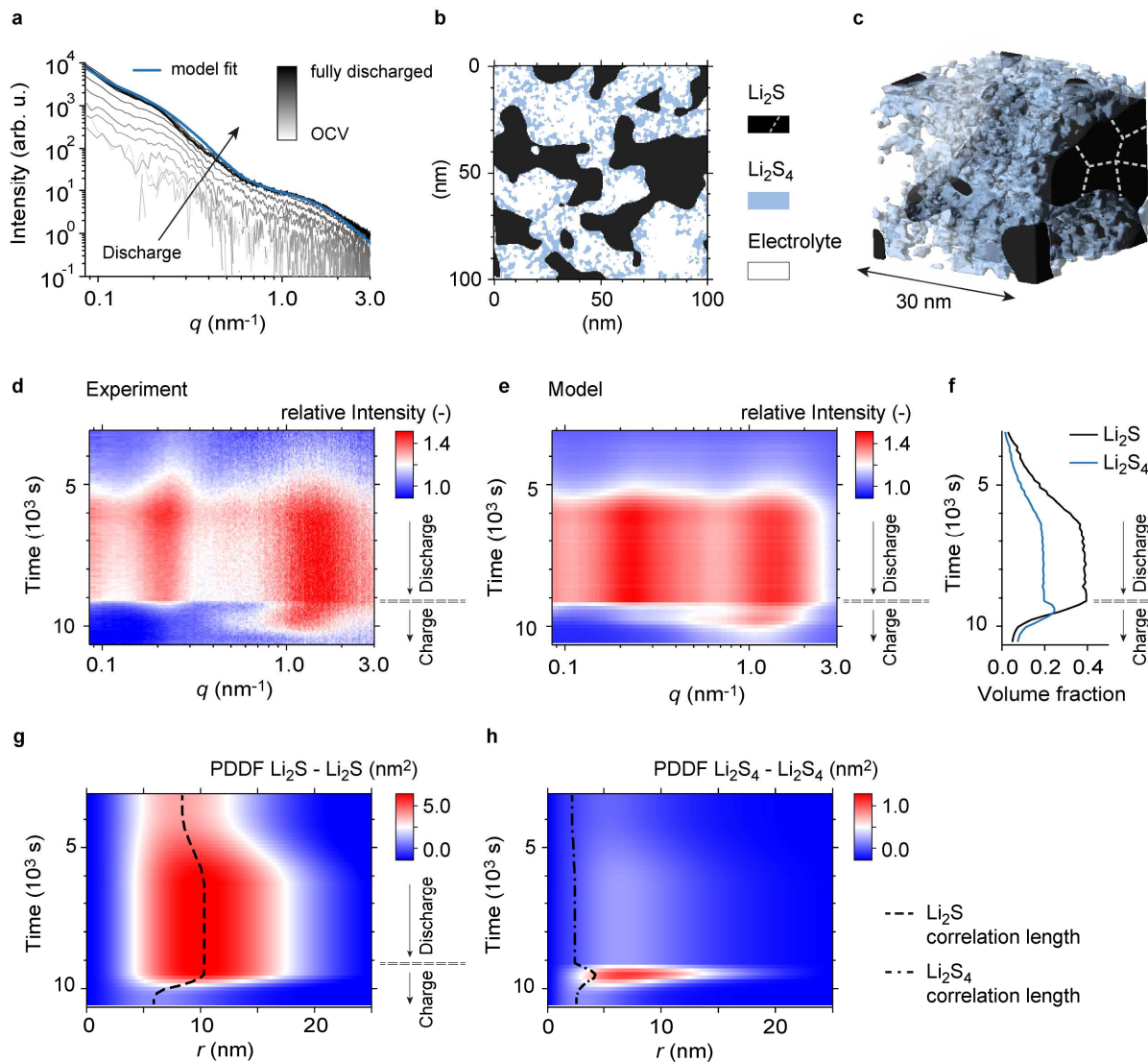
16 To remove the scattering contribution of carbon black and electrolyte structure factor from the evolving Li₂S /
17 Li₂S₄ composite structure, we subtract the SAXS intensity prior to discharge as well as a constant background
18 from all *in situ* SAXS intensities (Methods). The remaining, reduced SAXS intensities correspond to the Li₂S
19 / Li₂S₄ scattering contribution, assuming negligible correlations between Li₂S / Li₂S₄ and carbon black
20 structures (Fig. 4a).

21 By fitting the SAXS intensity of the fully discharged electrode (Fig. 4a), we extract parameters for (i) the feature
22 sizes of Li₂S and Li₂S₄, (ii) the respective volume fractions of Li₂S and Li₂S₄, and (iii) a parameter accounting
23 for the spatial correlation between the Li₂S and Li₂S₄ structures (Table S1). The latter parameter (δ , see
24 Methods) defines whether Li₂S₄ particles are preferably located close to the Li₂S surface ($\delta \rightarrow 0^\circ$) or randomly
25 distributed across cavities that form amongst the Li₂S particles ($\delta \rightarrow 90^\circ$). The value of $\delta = 45^\circ$ shows that
26 Li₂S₄ particles are growing in close proximity to the Li₂S crystallites. This is in line with the disproportionation
27 reaction in Equation 1 and Fig. 3a. With these parameters, we generate a 3D representation of the Li₂S/Li₂S₄
28 nanostructure on a 3D lattice shown in Fig. 4b (cross section) and Fig. 4c (3D visualization). This visualization
29 highlights the smaller size of Li₂S₄ particles compared to Li₂S particles, the Li₂S₄ growth in close proximity to
30 the solid Li₂S, and the mean aggregate size around 24 nm.

31 With the time-dependent input parameters described in Supplementary Note 2, we model the SAXS intensity
32 during discharge and charge. The salient features of the experimental *in situ* data (Fig. 4d) are reproduced
33 by the model (Fig. 4e) for the full discharge/charge cycle. Deviations between the model and experiment can
34 be explained by carbon-Li₂S/Li₂S₄ correlations, which were not considered here. The comparatively better
35 model fit for Li₂S/Li₂S₄ deposited on glassy carbon beads confirm this (Supplementary Fig. 5).

36 Fig. 4f shows the Li₂S and Li₂S₄ volumes as used in the time-dependent PGRF model. They are calculated
37 by multiplying the Li₂S and Li₂S₄ volume fractions ϕ_{Li_2S} and $\phi_{Li_2S_4}$ with the relative volume change of the Li₂S
38 / Li₂S₄ deposits V/V_{max} (both model inputs, see Supplementary Fig. 10). We see that the Li₂S₄ volume grows
39 at initial stages of charge, and so do the Li₂S₄ particles (high- q maximum shifting to smaller q as shown in
40 Fig. 4d). Li₂S₄ dissolution lags behind Li₂S dissolution during the entire charge, shifting relative volume
41 fractions towards Li₂S₄, and suggesting that Li₂S₄ is the driver for Li₂S dissolution.

42 The Li₂S and Li₂S₄ pair distance distribution functions (Fig. 4g-h) quantify the time evolution of the Li₂S and
43 Li₂S₄ structures in real-space. Note that the maxima for Li₂S₄ (white to red shading) do not track the mean
44 particle radius of around 1.25 nm (black dash-dotted line). This can be explained by the significant correlations
45 between the Li₂S₄ and Li₂S structure (quantified by the parameter $\delta = 45^\circ$). Hence Li₂S₄ particles preferably
46 grow next to the Li₂S crystallites, which is consistent with a disproportionation reaction (Equation 1).

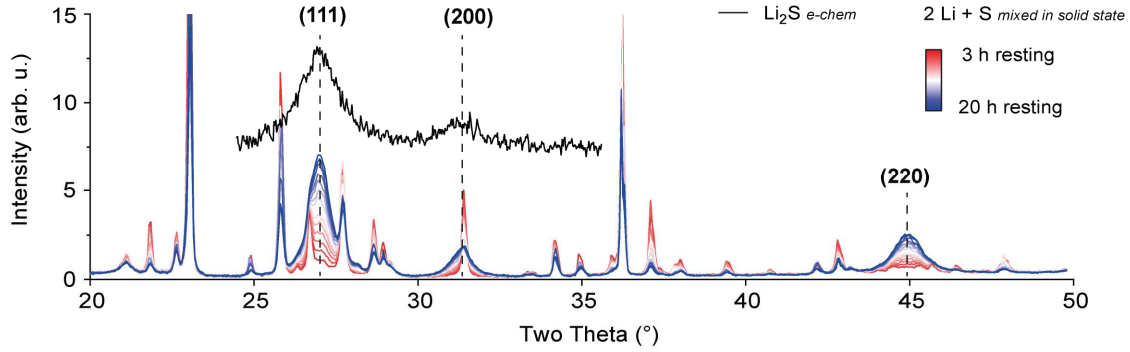


1
2 **Figure 4 | A stochastic SAXS model to describe the nanoscale phase evolution of Li_2S / Li_2S_4 deposits.** **A**, reduced
3 SAXS intensities versus scattering vector length q during potentiostatic discharge at 2.0 V vs. Li/Li^+ . The SAXS intensity
4 prior to discharge (at OCV) and hence the carbon scattering contribution was subtracted from the SAXS intensities shown
5 in Fig. 2a. The plurigaussian random field (PGRF) model fit is given in blue. **b-c**, The corresponding representative real
6 space model generated via PGRFs and the input parameters obtained from the model fit in **a**. **b** shows a 100 nm^2 cross
7 section, **c** a 3D visualization of a 30 nm^3 cut-out. White dashed lines indicate schematically that Li_2S aggregates consist
8 of individual Li_2S grains. **D**, Experimental relative SAXS intensity change as a function of time and scattering vector q
9 during potentiostatic discharge / charge. The data is equivalent to the data shown in Fig. 2d. **e**, Modelled relative SAXS
10 intensity change using the PGRF model and the time-dependent input parameters shown in Supplementary Note 2. **f**,
11 Li_2S and Li_2S_4 volume fractions as used in the time-dependent PGRF model multiplied by the relative volume change of
12 Li_2S / Li_2S_4 deposits V/V_{max} (see Supplementary Fig. 10). **g**, Li_2S – Li_2S pair distance distribution function (PDDF) as a
13 function of time and distance r , corresponding to the time-dependent PGRF model shown in **e**. **h**, Li_2S_4 – Li_2S_4 PDDF as a
14 function of time and distance r , corresponding to the time-dependent PGRF model shown in **e**. The dashed and dashed-
15 dotted black curves in **g-h** correspond to a Li_2S and Li_2S_4 particle correlation length, respectively, and serves as a guide
16 for the eye for the time-dependency of particle sizes. The correlation length is arbitrarily defined as the distance where the
17 correlation function equals 0.2 (Supplementary Fig. 6). Details are given in the methods section.

18 Solid-state disproportionation

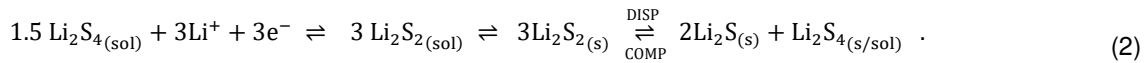
19 We next investigate whether the dis- and com-proportionation reactions can in principle occur in the solid
20 state. The relatively constant Li_2S crystallite sizes independent of the used electrolytes and experimental

1 conditions suggest diffusion-limitation dictated by the solid phase rather than by the electrolyte, and hence a
 2 solid-state process to be involved. We rolled crystalline sulphur onto a piece of Li metal in a molar ratio of 2:1
 3 under Ar atmosphere and recorded the XRD pattern of the resulting mixture from 3 to 20 hours after mixing
 4 (Fig. 5, details see Methods). The crystallite size obtained from the diffraction peak widths remained constant
 5 for the different resting times and similar to the Li₂S size obtained from electrochemical discharge (Fig. 5).
 6 This suggests that Li₂S during Li-S battery discharge is formed by solid-state disproportionation.



7
 8 **Figure 5 | Li₂S formation via solid-state disproportionation.** X-ray diffraction (XRD) pattern of solid Li mixed with solid
 9 S (in a molar ratio of 2:1) after different resting times at RT (red to blue solid lines). S and Li were mixed by rolling the solid
 10 S powder onto a piece of Li metal on a glass plate in inert Argon atmosphere. Next to the sharp S diffraction peaks, broader
 11 Li₂S diffraction peaks evolved. The Li₂S peaks show a similar width as the Li₂S obtained from electrochemical discharge
 12 (black solid line). The Scherrer crystallite size of the (111) peak is 7 nm for Li₂S obtained from electrochemical discharge
 13 and around 12 nm for Li₂S obtained by mixing solid S and Li. With increasing resting time, the Li₂S diffraction peaks grow,
 14 their width and the crystallite size remain constant. This indicates that Li₂S in Li-S batteries is formed via solid-state
 15 disproportionation.

16 This can be explained by expanding Equation 1 by the electron transfer process between Li₂S₄ and Li₂S₂,
 17 from which we obtain



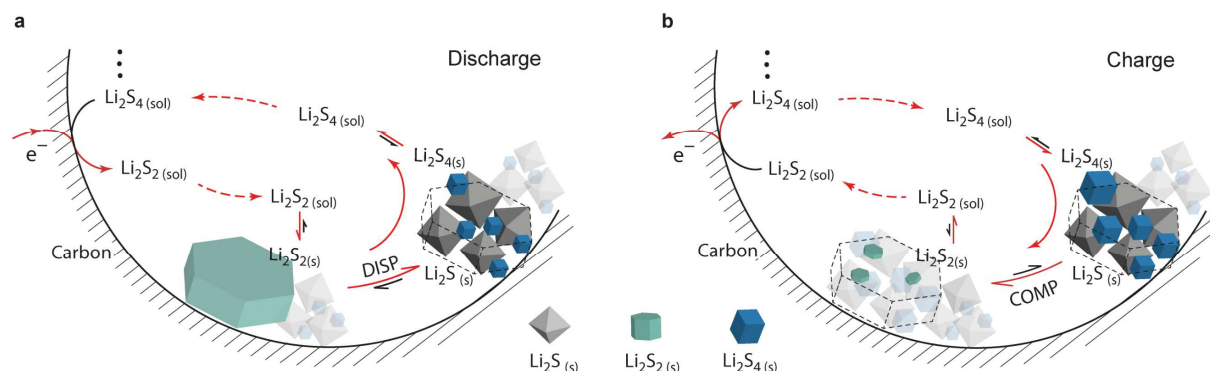
18 3Li₂S_{2(s)} denotes transient solid Li₂S₂ crystallites.

19 The processes in Equation 2 are illustrated in Fig. 6. Prior to disproportionation, the precipitation step
 20 3 Li₂S_{2(sol)} ⇌ 3Li₂S_{2(s)} forms transient solid Li₂S₂ crystallites, which determine the number density, size and
 21 shape of the final Li₂S/Li₂S₄ aggregates. We hypothesize that the crystalline Li₂S₂ is not detectable with
 22 WAXS/XRD as the Li₂S₂ are transient. Only under specific conditions transient, crystalline Li₂S₂ has been
 23 observed experimentally^{45,46}.

24 Disproportionation via transient solid Li₂S₂ explains why Li₂S deposits in Li-S batteries can form distinct single
 25 crystal-like shapes (e.g. platelets^{15,16}) of sizes beyond several 100 nm, where the primary Li₂S crystal size
 26 (as observed by XRD) is constantly around 10 nm. Further, it explains why Li₂S aggregate size and shape
 27 depend strongly on current³⁹ and solvent¹⁵, while the Li₂S primary crystallite size does not.

28 Alternative routes such as disproportionation in solution followed by precipitation (3 Li₂S_{2(sol)} ⇌ 2 Li₂S_(sol) +
 29 Li₂S_{4(sol)} ⇌ 2 Li₂S_(s) + Li₂S_{4(sol)}) appear unlikely given the unfavorable solvation of Li₂S. Upon discharge,
 30 Li₂S₄ is both the educt to form Li₂S₂ via electron transfer and the product of disproportionation. Upon charge,
 31 Li₂S₄ is both the product of Li₂S₂ oxidation and the educt of comproportionation. Hence, the very right hand
 32 side of Equation 2 feeds back to the very left. Except for the electron transfer step, all steps are equilibria.
 33 The direction of electron transfer will, therefore, create a net flow with the same direction in these equilibria;
 34 disproportionation (DISP) following reduction and comproportionation (COMP) following oxidation. Spatially,

1 electron transfer at the carbon surface and DISP/COMP at Li₂S surfaces (mostly inside porous deposits) are
 2 separated, requiring diffusive transport in between.



3
 4 **Figure 6 | The reversible DISP/COMP process during discharge/charge.** a, b, Processes and equilibria
 5 upon discharge (a) and charge (b). The mechanism centers around the DISP/COMP equilibrium $3 \text{Li}_2\text{S}_{2(s)} \rightleftharpoons (\text{Li}_2\text{S})_{2(s)} +$
 6 $\text{Li}_2\text{S}_{4(s/sol)}$. The net direction (red arrows) is set by the electron transfer step. Dashed arrows indicate diffusion. Solid Li₂S,
 7 Li₂S₂, and Li₂S₄ are illustrated according to their Wulff shapes⁴⁷.

8 According to Equation 2, some Li₂S₂ and Li₂S₄ will remain dissolved at the end of discharge. This is because
 9 neither is directly electrochemically converted to Li₂S. This is in accord with a relative Li₂S-to-Li₂S₄ volume
 10 fraction of 2:1 (Fig. 4f). The 2:1 Li₂S:Li₂S₄ molar ratio from disproportionation in Equation 1 would result in a
 11 Li₂S:Li₂S₄ volume ratio of 0.7:1.

12 During charge, dissolved Li₂S₂ is electrochemically oxidized to Li₂S₄(sol). Hence, solid Li₂S₄(s) can still grow (as
 13 seen in Fig. 4d). Li₂S₄(sol) thus acts as mediator to oxidize and dissolve Li₂S without any electronic conduction
 14 through Li₂S deposits. Galvanostatic charging of a discharged electrode after washing and drying confirms
 15 this (Supplementary Fig. 7). Since washing removes part of the dissolved Li₂S₂ and Li₂S₄, charging after
 16 washing leads to higher overpotentials at initial stages of charge.⁴⁸ Without the dissolved PSs serving as
 17 mediators, initial charging requires the direct oxidation of Li₂S, likely at Li₂S/C/electrolyte three-phase
 18 boundaries.

19 As the SAXS data modelling may involve systematic errors, it is important to understand which outcomes are
 20 based on model-free experimental results. The fact that Li₂S forms via disproportionation is clear. It is verified
 21 by in situ WAXS, SEM and ex situ XRD of PS powders and Li metal mixed with solid sulphur. Details of the
 22 nanostructure quantified via the stochastic SAXS model on the other hand need further refinement. Instead
 23 of Li₂S₄, in principle, other solid higher-order PSs, i.e. other disproportionation reactions than Equation 1 may
 24 explain the high-*q* SAXS intensity shoulder. Given the consistency of the derived mechanism with all
 25 experimental data and the possible disproportionation reactions^{20,41}, alternative SAXS data interpretations
 26 remain highly unlikely (see Supplementary Note 1).

27 Conclusions

28 In conclusion, we provide direct experimental evidence that solid Li₂S in Li-S batteries forms via precipitation
 29 of short-chain polysulfides (such as Li₂S₂) and subsequent solid-state disproportionation or phase separation.
 30 Besides solid Li₂S, the SAXS data indicate the formation of a second solid PS phase (such as Li₂S₄), with
 31 smaller particle size. During charge, the particles of this second phase initially grow while Li₂S already
 32 disappears. The behavior is consistent with a DISP/COMP equilibrium between the short- and longer-chain PS
 33 plus a longer-chain PS. Electron transfer interconverts the short- and longer-chain PSs and its direction
 34 determines the net flux through the equilibrium, giving rise to Li₂S formation/dissolution on discharge/charge
 35 without the need for electron transport across the insulating Li₂S.

1 Converting Li_2S_2 to Li_2S affords half of the theoretical capacity of Li-S cells and is – as we show – a chemical
2 rather than electrochemical reaction. It means that discharge capacity of a Li-S battery cathode is limited by
3 mass transport^{16,17} through the tortuous network of Li_2S / Li_2S_4 / carbon pores rather than electron transport
4 through a passivating surface film¹¹ (note that macroscopic PS transport through the separator and PS
5 reactions at the anode might be limiting as well in practical systems). Knowing this, shifts paradigms of how
6 to control the discharge capacity. The achievable Li_2S pore filling and hence the discharge capacity is not
7 only limited by the electrolyte solvation strength, but equally by the applied current density and the mobility of
8 the reactive species. Theoretical sulphur capacities may never be achieved as a certain amount of higher-
9 order PSs remains in solution and/or as a second solid phase. Concerning the initial overpotential during
10 charging, remaining PSs are beneficial as they mediate charge transfer via solution, bypassing the insulating
11 Li_2S .

12 Given the known relation between electrolyte solvation and Li_2S morphology^{13,15} (i.e., Li_2S nucleation and
13 growth), we believe that solvation energies influence on the one hand Li_2S_2 crystallization in terms of
14 nucleation and size/shape, of which the Li_2S deposits form replicas. On the other hand, the electrolyte
15 determines redissolution and diffusion of the longer-chain DISP product, which is critical for approaching
16 theoretical capacities.

17 More broadly, the solid-state disproportionation mechanism indicates solid state DISP of precipitated Li_2S_2 to
18 have similar kinetics to precipitation of Li_2S_2 and redissolution of Li_2S_4 . Solid state DISP requires Li
19 redistribution from the Li_2S_2 into the Li_2S and Li_2S_4 phases, which appears sufficiently facile on a scale of up
20 to 10 nm, as indicated by the Li_2S crystallite sizes. This implies that solid-state S-to- Li_2S conversion (SSC) is
21 possible at practical rates if S/ Li_2S structures are properly engineered, which is a very important message for
22 all Li-S design strategies that avoid the polysulfide shuttling problem by utilizing SSC, but so far struggled to
23 convert practical S amounts.

24

1 **Methods**

2 **Materials**

3 As cathode material we used a high-surface area carbon black (Ketjenblack, EC-600JD, ANR Technologies)
4 with a BET area of $1400 \text{ m}^2 \text{ g}^{-1}$. The free-standing film electrodes were prepared by mixing carbon with
5 polytetrafluoroethylene (PTFE, 60 mass% suspension in water, Aldrich) at 90/10 mass ratio with isopropanol.
6 The resulting dough-like material was rolled to a 50-70 μm thick film, washed in acetone/ H_2O mixture and
7 finally dried at $120 \text{ }^\circ\text{C}$ under vacuum overnight. As catholyte we used a solution of $0.5 \text{ M Li}_2\text{S}_8 + 1 \text{ M lithium}$
8 $\text{bis(trifluoromethane)sulfonimide (LiTFSI) + 0.4 M lithium nitrate (LiNO}_3\text{)}$ in diethylene glycol dimethyl ether
9 (2G). In Supplementary Fig. 1 we show in situ SAXS/WAXS data using a sulphur infiltrated carbon black
10 cathode (ENSACO 350G/S) with a solution of $1 \text{ M LiTFSI} + 0.1 \text{ M LiNO}_3$ in 1:1 (v:v) 1,3-dioxolan (DOL) +
11 tetraethylene glycol dimethyl ether (TEGDME) as electrolyte. The ENSACO 350G carbon (Imerys) / sulphur
12 composite was prepared in a C:S = 1:2 mass ratio by melt infiltration under Ar atmosphere at $155 \text{ }^\circ\text{C}$. The
13 electrode was prepared by adding Printex (Degussa) conductivity additive and PVdF binder to the C/S
14 composite in a mass ratio of 1:1:8. All solvents were used as received and dried under freshly activated
15 Molecular Sieves (type 4 Å). All salts were dried at elevated temperature ($90 \text{ }^\circ\text{C}$) and reduced pressure.

16 Lithium polysulfide powders were synthesized by mixing a stoichiometric amount of elemental sulphur (Sigma
17 Aldrich) and lithium metal (FMC) in excess of dried THF (the THF was dried in a multistep process using
18 Al_2O_3 , molecular sieves, and distillation, after which the water content was measured by Karl Fischer titration
19 (Mettler Toledo, G20) and kept below 2 ppm.). The synthesis procedure was conducted in an argon filled dry
20 box with controlled levels of water and oxygen content (below 0.1 ppm). The mixture was stirred at slightly
21 elevated temperatures ($50 \text{ }^\circ\text{C}$) until all the reactants dissolved. THF was then removed under reduced
22 pressure to obtain dry polysulfide powders.

23 The solid $2 \text{ Li} + \text{S}$ mixture was prepared by rolling fine sulphur powder (large S crystals crushed with mortar
24 and pestle) onto a thin piece of Li metal on a glass plate in inert atmosphere. The Li and S mass correspond
25 to a molar ratio of 2:1. After a short time of rolling the Li/S piece was turning brittle, indicating immediate Li_2S
26 crystal formation.

27 **Experimental**

28 In situ SAXS/WAXS and XRD measurements were carried out with a commercial electrochemical in situ
29 scattering cell (BatterycellSAXS, Anton Paar, Austria). We used polytetrafluoroethylene (PTFE) X-ray
30 windows due to their chemical stability and relatively low background in the SAXS regime. The small diameter
31 of the windows (2 mm) ensures a relatively equal pressure distribution across the cell assembly. It consisted
32 of a Li metal anode, a Celgard separator, a Freudenberg (FS 2125) separator, a carbon black cathode, and
33 an Aluminium grid current collector. The X-ray beam irradiates all cell materials; reversible and significant
34 structural changes are only detected in the cathode. A Biologic SP240potentiostat/galvanostat was used for
35 electrochemical cycling.

36 In situ SAXS/WAXS measurements were carried out on the Austrian SAXS beamline at the Synchrotron
37 ELETTRA³⁶ (Trieste, Italy) using an X-ray wavelength of 0.154 nm and a Pilatus 1M SAXS and Pilatus 100K
38 WAXS detector (Dectris, Switzerland). During potentiostatic discharge / charge measurements, SAXS and
39 WAXS patterns were collected with 1 s exposure time (to avoid radiation damage) and 60 s period (to avoid
40 huge amounts of data). We discharged the cell at 2.0 V vs. Li/Li^+ for 2.5 hours (giving a capacity of 1520 mAh
41 g^{-1}) and charged it at 2.45 V vs. Li/Li^+ for maximum 2.5 hours (to reverse the capacity of 1520 mAh g^{-1}). In
42 situ SAXS data shown in Supplementary Fig. 1 were recorded on a laboratory SAXS/WAXS instrument
43 (SAXSpoint 2.0, Anton Paar, Austria) with an EIGER2 R 1M area detector (Dectris, Switzerland) and a time
44 resolution of XX min. All recorded SAXS patterns were azimuthally averaged and normalized by transmission
45 values. The SAXS background intensity was recorded separately for each cell after removing the cathode.
46 The averaged and normalized background intensity was then subtracted from all recorded *in situ* SAXS

1 curves. The azimuthally averaged 2D *in situ* WAXS data were corrected by subtracting the WAXS intensity
2 prior to discharge (at OCV).

3 Scanning Electron Microscopy (SEM) images were collected with a Hitachi SU-8200 at 5.0 kV acceleration
4 voltage using a secondary electron detector. Ex situ XRD (and SAXS) measurements (Fig. 3b, Fig. 5,
5 Supplementary Figs. 2, 4) were carried out on a Rigaku SmartLab 9 kW System, with rotating Cu anode and
6 2D solid state detector (HyPix-3000 SL).

7 **In situ SAXS data modelling via plurigaussian random fields**

8 The SAXS intensity of the discharged cathode can be split into three terms,

$$I(q) = I_{\text{Li}_2\text{S},\text{Li}_2\text{S}_4}(q) + I_{\text{C}}(q) + BG. \quad (3)$$

9 The first term $I_{\text{Li}_2\text{S},\text{Li}_2\text{S}_4}(q)$ corresponds to the scattering contribution of the $\text{Li}_2\text{S} / \text{Li}_2\text{S}_4$ structure, the second
10 term $I_{\text{C}}(q)$ to the scattering contribution of the electrolyte-filled carbon structure and the third background term
11 to the constant (low- q) intensity of electrolyte (and carbon) atomic structure factor. Correlations between
12 carbon black and the $\text{Li}_2\text{S} / \text{Li}_2\text{S}_4$ structure are neglected (see discussion in Supplementary Note 1 and
13 Supplementary Fig. 5).

14 To separate the SAXS intensity of the $\text{Li}_2\text{S} / \text{Li}_2\text{S}_4$ structure we subtract $I_{\text{C}}(q)$, i.e., the SAXS intensity
15 measured prior to discharge at OCV. Further, we subtract the electrolyte (and carbon) structure factor
16 background BG by a Porod background subtraction in a q -range from 3–5 nm^{-1} .

17 The SAXS intensity of the $\text{Li}_2\text{S} / \text{Li}_2\text{S}_4$ nanostructure (Fig. 4a) can be written as

$$I_{\text{Li}_2\text{S},\text{Li}_2\text{S}_4}(q) = K (V/V_{\text{max}}) [A q^{-4} + I_{\text{PGRF}}(q)], \quad (4)$$

18 with K being a constant that depends on instrumental parameters, such as detector efficiency and irradiated
19 sample volume, and V/V_{max} the relative volume of the deposited $\text{Li}_2\text{S} / \text{Li}_2\text{S}_4$ nanostructure. The first power
20 law term stems from the large $\text{Li}_2\text{S} (\text{Li}_2\text{S}_4)$ agglomerates beyond 100 nm (see SEM images in Fig. 1c. Given
21 their large expansion, the SAXS intensity in the measured q range is proportional to q^{-4} (Porod decay). The
22 second term accounts for the $\text{Li}_2\text{S} / \text{Li}_2\text{S}_4$ nanostructure in the size regime between 1 to 50 nm and is modelled
23 via plurigaussian random fields, as described further below. The least square error sum is minimized by
24 particle swarm optimization⁴⁹ with reasonable parameter constraints. Deviations between model fit (blue curve
25 in Fig. 4a) and experimental data (black curve in Fig. 4a) can be explained by carbon black – $\text{Li}_2\text{S}/\text{Li}_2\text{S}_4$
26 correlations. $\text{Li}_2\text{S} / \text{Li}_2\text{S}_4$ nanostructures deposited on a planar Glassy carbon substrate with negligible cross
27 correlations show an improved fit quality (Supplementary Fig. 5).

28 Time-dependent SAXS intensity change during discharge and charge are modelled by using the fit
29 parameters of the model fit to the fully discharged electrode in Fig. 4a (Table S1) as a starting point. All input
30 parameters for the modelled *in situ* SAXS data are given in Supplementary Note 2.

31 We model the reduced *in situ* SAXS data $I_{\text{PGRF}}(q)$ using the concept of plurigaussian random fields (PGRF)⁴⁴.
32 This allows retrieving 3D real space models of the solid $\text{Li}_2\text{S} / \text{Li}_2\text{S}_4$ nanostructure during discharge and charge
33 (Fig. 4). A detailed theoretical description of the PGRF method is given by Gommès et al.⁴⁴.

34 The SAXS intensity $I_{\text{PGRF}}(q)$ is the Fourier transform of the electron density correlation function $C(r)$

$$I_{\text{PGRF}}(q) = \int_0^\infty C(r) \frac{\sin(qr)}{qr} 4\pi r^2 dr. \quad (5)$$

35 $C(r)$ for our three-phase system consisting of phases Li_2S , Li_2S_4 , Electrolyte (EL) can be written as

$$\begin{aligned}
C(r) = & (\rho_{\text{Li}_2\text{S}} - \rho_{\text{Li}_2\text{S}_4})(\rho_{\text{Li}_2\text{S}} - \rho_{\text{EL}})[P_{\text{Li}_2\text{S Li}_2\text{S}}(r) - \phi_{\text{Li}_2\text{S}}^2] \\
& + (\rho_{\text{Li}_2\text{S}_4} - \rho_{\text{Li}_2\text{S}})(\rho_{\text{Li}_2\text{S}_4} - \rho_{\text{EL}})[P_{\text{Li}_2\text{S}_4 \text{Li}_2\text{S}_4}(r) - \phi_{\text{Li}_2\text{S}_4}^2] \\
& + (\rho_{\text{EL}} - \rho_{\text{Li}_2\text{S}})(\rho_{\text{EL}} - \rho_{\text{Li}_2\text{S}_4})[P_{\text{EL EL}}(r) - \phi_{\text{EL}}^2].
\end{aligned} \tag{6}$$

- 1 Here, ρ_i is the electron density, ϕ_i the volume fraction and $P_{ii}(r)$ the two-point correlation function of phase i .
2 Using clipped Gaussian random fields, a 3D model of a two-phase nanopore structure can be generated from
3 a fit to the structure's experimental SAXS intensity⁵⁰⁻⁵³. Plurigaussian random fields use a second Gaussian
4 random field to model SAXS intensities and 3D real space structures of disordered three-phase systems. A
5 Gaussian random field $Y(\mathbf{x})$ is the sum of cosine waves with wave vector lengths distributed according to
6 their power spectral density $f_Y(k)$ and phase factors φ_i randomly distributed between 0 and 2π ^{44,50,54,55}.

$$Y(\mathbf{x}) = \sqrt{\frac{2}{N}} \sum_{i=1}^N \cos(\mathbf{k}_i \cdot \mathbf{x} - \varphi_i) \tag{7}$$

- 7 A suitable analytic two-point correlation function of the GRF is⁵³

$$g_Y(r) = \frac{1}{\cosh(r/l_Y)} \cdot \frac{\sin(2\pi r/d_Y)}{(2\pi r/d_Y)}, \tag{8}$$

- 8 where l_Y is a correlation parameter related to the mean size of the structure and d_Y a parameter accounting
9 for ordering effects via the second oscillation term. Equation 7 translates into the following analytic expression
10 for the power spectral density:

$$f_Y(k) = \frac{k}{\pi} l_Y d_Y \frac{\sinh(\pi k l_Y/2) \sinh(\pi^2 l_Y/d_Y)}{\cosh(\pi k l_Y) + \cosh(2\pi^2 l_Y/d_Y)}. \tag{9}$$

- 11 To generate a two-phase porous structure from the GRF, we define the threshold values α for the Gaussian
12 distributed $Y(\mathbf{x})$ values. All spatial coordinates \mathbf{x} with $\alpha < Y(\mathbf{x}) \leq \infty$ are assigned to the pore space (i.e.
13 phase $\text{Li}_2\text{S}_4 + \text{EL}$); all other coordinates to the Li_2S skeleton. The two threshold values are related to the Li_2S
14 volume fraction $\phi_{\text{Li}_2\text{S}}$ via:

$$\phi_{\text{Li}_2\text{S}} = \frac{1}{\sqrt{2\pi}} \int_{\alpha}^{\infty} \exp\left(-\frac{t^2}{2}\right) dt. \tag{10}$$

- 15 To model SAXS intensities and real space structures of the three phase system, we generate a second
16 independent GRF $Z(\mathbf{x})$ using the same correlation function (Equation 8-9) with different input parameters l_Z
17 and d_Z (Supplementary Fig. 8c). The Li_2S_4 phase with the volume fraction $\phi_{\text{Li}_2\text{S}_4}$ is generated by cutting $Z(\mathbf{x})$
18 and $Y(\mathbf{x})$ according to Equation 11 and the cut-offs visualized in Supplementary Fig. 8.

$$\phi_{\text{Li}_2\text{S}_4} = \iint_{(Y,Z) \in D_{\text{Li}_2\text{S}_4}} \frac{1}{2\pi} \exp\left(-\frac{Y^2 + Z^2}{2}\right) dY dZ \tag{11}$$

- 19 The two-point correlation functions of the phase Li_2S_4 (equivalent for Li_2S) are calculated via

$$P_{\text{Li}_2\text{S}_4 \text{Li}_2\text{S}_4} = \int_{D_{\text{Li}_2\text{S}_4}} dY_1 dZ_1 \int_{D_{\text{Li}_2\text{S}_4}} dY_2 dZ_2 G_{g_Y(r)}(Y_1, Y_2) G_{g_Z(r)}(Z_1, Z_2) \tag{12}$$

1 with $G_g(Y_1, Y_2)$ being the bivariate Gaussian distribution with mean 0, variance 1, and covariance G . Their
 2 calculation via Hermite polynomials is described in Ref. ⁴⁴. Depending on the angle δ and the $\text{Li}_2\text{S}_4/\text{EL}$
 3 boundary line in Supplementary Fig. 8d-f, the morphology of the Li_2S_4 phase will be different. The Li_2S_4 phase
 4 will perfectly cover/wet the Li_2S phase in form of a thin film if $\delta \rightarrow 0$ (Supplementary Fig. 8d,g). In contrast, for
 5 an $\text{Li}_2\text{S}_4/\text{EL}$ boundary parallel to the Y -axis ($\delta \rightarrow \pi/2$) the Li_2S_4 (EL) structure inside the Li_2S cavities is
 6 statistically independent from the Li_2S structure (Supplementary Fig. 8f,i). Inserting Equation 12 into
 7 Equation 5-6 gives the corresponding scattering intensities (Fig. 4).

8 The modelled relative SAXS intensity change (Fig. 4e) is obtained by calculating $I_{\text{Li}_2\text{S}, \text{Li}_2\text{S}_4}(q)$ via Equation 4
 9 using the fit parameters shown in Supplementary Fig. 10 and adding $I_C(q) + BG$ (i.e. the experimental SAXS
 10 intensity at OCV). Finally, the generated SAXS intensities are normalized by the modeled SAXS intensity at
 11 $t = 0$, prior to discharge.

12 The pair distance distribution functions $p_{XX}(r)$ of phase X in Fig. 4g, h are calculated by normalizing the two-
 13 point correlation function $P_{XX}(r)$ (Equation 13).

$$p_{XX}(r) = r^2 [P_{XX}(r) - P_{XX}(r \rightarrow \infty)] / [P_{XX}(r = 0) - P_{XX}(r \rightarrow \infty)] \quad (13)$$

14 The correlation lengths of Li_2S and Li_2S_4 structures are arbitrarily taken as the distance where the normalized
 15 correlation function $[P_{XX}(r) - P_{XX}(r \rightarrow \infty)] / [P_{XX}(r = 0) - P_{XX}(r \rightarrow \infty)]$ has decayed to a value of 0.2 (see
 16 Supplementary Fig. 6).

17

18

1 **Data availability**

2 The data that support the findings of this study are available from the corresponding authors on request.

3

4 **Code availability**

5 The codes used for in situ SAXS data analysis and stochastic modelling are available from the corresponding
6 author C.P. on request.

References

- 1 Choi, J. W. & Aurbach, D. Promise and reality of post-lithium-ion batteries with high energy densities. *Nature Review Materials* **1**, 16013, (2016).
- 2 Bresser, D., Passerini, S. & Scrosati, B. Recent progress and remaining challenges in sulfur-based lithium secondary batteries – a review. *Chemical Communications* **49**, 10545-10562, (2013).
- 3 Pang, Q., Liang, X., Kwok, C. Y. & Nazar, L. F. Advances in lithium–sulfur batteries based on multifunctional cathodes and electrolytes. *Nat. Energy* **1**, 16132, (2016).
- 4 Bruce, P. G., Freunberger, S. A., Hardwick, L. J. & Tarascon, J.-M. Li-O₂ and Li-S batteries with high energy storage. *Nat. Mater.* **11**, 19-29, (2012).
- 5 Borchardt, L., Oschatz, M. & Kaskel, S. Carbon Materials for Lithium Sulfur Batteries—Ten Critical Questions. *Chem.: Eur. J.* **22**, 7324-7351, (2016).
- 6 Urbonaitė, S., Poux, T. & Novák, P. Progress Towards Commercially Viable Li–S Battery Cells. *Advanced Energy Materials* **5**, 1500118, (2015).
- 7 Wild, M. *et al.* Lithium sulfur batteries, a mechanistic review. *Energy Environ. Sci.* **8**, 3477-3494, (2015).
- 8 Xu, R., Lu, J. & Amine, K. Progress in Mechanistic Understanding and Characterization Techniques of Li-S Batteries. *Advanced Energy Materials* **5**, 1500408, (2015).
- 9 Lang, S.-Y. *et al.* Insight into the Interfacial Process and Mechanism in Lithium–Sulfur Batteries: An In Situ AFM Study. *Angew. Chem.* **55**, 15835-15839, (2016).
- 10 Barchasz, C., Leprêtre, J.-C., Alloin, F. & Patoux, S. New insights into the limiting parameters of the Li/S rechargeable cell. *Journal of Power Sources* **199**, 322-330, (2012).
- 11 Fan, F. Y., Carter, W. C. & Chiang, Y.-M. Mechanism and Kinetics of Li₂S Precipitation in Lithium–Sulfur Batteries. *Adv. Mater.* **27**, 5203-5209, (2015).
- 12 Barchasz, C. *et al.* Lithium/Sulfur Cell Discharge Mechanism: An Original Approach for Intermediate Species Identification. *Anal. Chem.* **84**, 3973-3980, (2012).
- 13 Yang, B. *et al.* Critical Role of Anion Donicity in Li₂S Deposition and Sulfur Utilization in Li-S Batteries. *ACS Appl. Mater. Interfaces* **11**, 25940-25948, (2019).
- 14 Chu, H. *et al.* Achieving three-dimensional lithium sulfide growth in lithium-sulfur batteries using high-donor-number anions. *Nat. Commun.* **10**, 188, (2019).
- 15 Li, Z., Zhou, Y., Wang, Y. & Lu, Y.-C. Solvent-Mediated Li₂S Electrodeposition: A Critical Manipulator in Lithium–Sulfur Batteries. *Advanced Energy Materials* **9**, 1802207, (2019).
- 16 Drvarič Talian, S. *et al.* Which Process Limits the Operation of a Li–S System? *Chemistry of Materials* **31**, 9012-9023, (2019).
- 17 Zhang, T., Marinescu, M., Walus, S., Kovacik, P. & Offer, G. J. What Limits the Rate Capability of Li-S Batteries during Discharge: Charge Transfer or Mass Transfer? *J. Electrochem. Soc.* **165**, A6001-A6004, (2018).
- 18 Zhang, T., Marinescu, M., Walus, S. & Offer, G. J. Modelling transport-limited discharge capacity of lithium-sulfur cells. *Electrochim. Acta* **219**, 502-508, (2016).
- 19 Aetukuri, N. B. *et al.* Ion Pairing Limits Crystal Growth in Metal–Oxygen Batteries. *ACS Energy Letters* **3**, 2342-2348, (2018).
- 20 Lu, Y.-C., He, Q. & Gasteiger, H. A. Probing the Lithium–Sulfur Redox Reactions: A Rotating-Ring Disk Electrode Study. *The Journal of Physical Chemistry C* **118**, 5733-5741, (2014).
- 21 Conder, J. *et al.* Direct observation of lithium polysulfides in lithium–sulfur batteries using operando X-ray diffraction. *Nat. Energy* **2**, 17069, (2017).
- 22 Cañas, N. A., Wolf, S., Wagner, N. & Friedrich, K. A. In-situ X-ray diffraction studies of lithium–sulfur batteries. *Journal of Power Sources* **226**, 313-319, (2013).
- 23 Dominko, R. *et al.* Polysulfides Formation in Different Electrolytes from the Perspective of X-ray Absorption Spectroscopy. *Journal of The Electrochemical Society* **165**, A5014-A5019, (2017).
- 24 Patel, M. U. M. *et al.* Li-S Battery Analyzed by UV/Vis in Operando Mode. *ChemSusChem* **6**, 1177-1181, (2013).
- 25 Lowe, M. A., Gao, J. & Abruña, H. D. Mechanistic insights into operational lithium–sulfur batteries by in situ X-ray diffraction and absorption spectroscopy. *RSC Adv.* **4**, 18347-18353, (2014).
- 26 Cañas, N. A. *et al.* Investigations of lithium–sulfur batteries using electrochemical impedance spectroscopy. *Electrochimica Acta* **97**, 42-51, (2013).
- 27 Marceau, H. *et al.* In operando scanning electron microscopy and ultraviolet–visible spectroscopy studies of lithium/sulfur cells using all solid-state polymer electrolyte. *J. Power Sources* **319**, 247-254, (2016).
- 28 Yu, S.-H. *et al.* Direct visualization of sulfur cathodes: new insights into Li–S batteries via operando X-ray based methods. *Energy Environ. Sci.* **11**, 202-210, (2018).
- 29 Tonin, G. *et al.* Multiscale characterization of a lithium/sulfur battery by coupling operando X-ray tomography and spatially-resolved diffraction. *Sci. Rep.* **7**, 2755, (2017).
- 30 Schröder, D. *et al.* In operando X-ray tomography for next-generation batteries: a systematic approach to monitor reaction product distribution and transport processes. *J. Phys. D* **49**, 404001, (2016).
- 31 Glatter, O. & Kratky, O. *Small angle X-ray scattering*. 17-51 (Academic Press Inc. Ltd., 1982).
- 32 Risse, S., Härk, E., Kent, B. & Ballauff, M. Operando Analysis of a Lithium/Sulfur Battery by Small-Angle Neutron Scattering. *ACS Nano* **13**, 10233-10241, (2019).
- 33 Prehal, C. *et al.* Persistent and reversible solid iodine electrodeposition in nanoporous carbons. *Nature Communications* **11**, 4838, (2020).

1 34 Prehal, C. *et al.* In situ small angle X-ray scattering reveals solution phase discharge of Li-O₂ batteries
2 with weakly solvating electrolytes. *PNAS* **118**, e2021893118, (2021).
3 35 Prehal, C. *et al.* Quantification of ion confinement and desolvation in nanoporous carbon supercapacitors
4 with modelling and in situ X-ray scattering. *Nature Energy* **2**, 16215, (2017).
5 36 Amenitsch, H. *et al.* First performance assessment of the small-angle X-ray scattering beamline at
6 ELETTRA. *Journal of Synchrotron Radiation* **5**, 506-508, (1998).
7 37 Gebauer, D., Kellermeier, M., Gale, J. D., Bergström, L. & Cölfen, H. Pre-nucleation clusters as solute
8 precursors in crystallisation. *Chemical Society Reviews* **43**, 2348-2371, (2014).
9 38 Thanh, N. T. K., Maclean, N. & Mahiddine, S. Mechanisms of Nucleation and Growth of Nanoparticles in
10 Solution. *Chemical Reviews* **114**, 7610-7630, (2014).
11 39 Kong, L. *et al.* Current-density dependence of Li₂S/Li₂S₂ growth in lithium-sulfur batteries. *Energy &*
12 *Environmental Science* **12**, 2976-2982, (2019).
13 40 Patel, M. U. M. *et al.* X-ray Absorption Near-Edge Structure and Nuclear Magnetic Resonance Study of
14 the Lithium-Sulfur Battery and its Components. *ChemPhysChem* **15**, 894-904, (2014).
15 41 Wujcik, K. H. *et al.* Fingerprinting Lithium-Sulfur Battery Reaction Products by X-ray Absorption
16 Spectroscopy. *Journal of The Electrochemical Society* **161**, A1100-A1106, (2014).
17 42 See, K. A. *et al.* Ab Initio Structure Search and in Situ ⁷Li NMR Studies of Discharge Products in the Li-S
18 Battery System. *Journal of The American Chemical Society* **136**, 16368-16377, (2014).
19 43 Drvarič Talian, S. *et al.* Fluorinated Ether Based Electrolyte for High-Energy Lithium-Sulfur Batteries: Li+
20 Solvation Role Behind Reduced Polysulfide Solubility. *Chemistry of Materials* **29**, 10037-10044, (2017).
21 44 Gommès, C. Three-dimensional reconstruction of liquid phases in disordered mesopores using in situ
22 small-angle scattering. *J. Appl. Crystallogr.* **46**, 493-504, (2013).
23 45 Paolella, A. *et al.* Transient existence of crystalline lithium disulfide Li₂S₂ in a lithium-sulfur battery. *Journal*
24 *of Power Sources* **325**, 641-645, (2016).
25 46 Partovi-Azar, P., Kühne, T. D. & Kaghazchi, P. Evidence for the existence of Li₂S₂ clusters in lithium-
26 sulfur batteries: ab initio Raman spectroscopy simulation. *Physical Chemistry Chemical Physics* **17**,
27 22009-22014, (2015).
28 47 Park, H., Koh, H. S. & Siegel, D. J. First-Principles Study of Redox End Members in Lithium-Sulfur
29 Batteries. *The Journal of Physical Chemistry C* **119**, 4675-4683, (2015).
30 48 Ye, H., Li, M., Liu, T., Li, Y. & Lu, J. Activating Li₂S as the Lithium-Containing Cathode in Lithium-Sulfur
31 Batteries. *ACS Energy Letters* **5**, 2234-2245, (2020).
32 49 Kennedy, J. & Eberhart, R. in *Proceedings of ICNN'95 - International Conference on Neural Networks.*
33 1942-1948 vol.1944.
34 50 Gommès, C. J. Stochastic models of disordered mesoporous materials for small-angle scattering analysis
35 and more. *Microporous Mesoporous Mater.* **257**, 62-78, (2018).
36 51 Gommès, C. J. & Roberts, A. P. Structure development of resorcinol-formaldehyde gels: Microphase
37 separation or colloid aggregation. *Phys. Rev. E* **77**, 041409, (2008).
38 52 Prehal, C. *et al.* Comparing pore structure models of nanoporous carbons obtained from small angle X-
39 ray scattering and gas adsorption. *Carbon* **152**, 416-423, (2019).
40 53 Prehal, C. *et al.* A carbon nanopore model to quantify structure and kinetics of ion electrosorption with in
41 situ small angle X-ray scattering. *Phys. Chem. Chem. Phys.* **19**, 15549, (2017).
42 54 Roberts, A. P. Statistical reconstruction of three-dimensional porous media from two-dimensional images.
43 *Phys. Rev. E* **56**, 3203-3212, (1997).
44 55 Berk, N. Scattering properties of the leveled-wave model of random morphologies. *Phys. Rev. A* **44**, 5069,
45 (1991).

46

47

1 **Acknowledgements**

2 This project has received funding from the European Union's Horizon 2020 research and innovation program
3 under the Marie Skłodowska-Curie grant NanoEvolution, grant agreement No 894042. The authors
4 acknowledge TU Graz for support through the Lead Project LP-03. Likewise, the use of SOMAPP Lab, a core
5 facility supported by the Austrian Federal Ministry of Education, Science and Research, the Graz University
6 of Technology, the University of Graz, and Anton Paar GmbH is acknowledged. S.D.T, A.V. and R.D.
7 acknowledge the financial support by the Slovenian Research Agency (ARRS) research core funding P2-
8 0393. Furthermore, A.V. acknowledge the funding from the Slovenian Research Agency, research project Z2-
9 1863. S.A.F. is indebted to IST Austria for support.

10

11 **Author Contributions**

12 C.P. carried out *in situ* scattering, electrochemical and electron microscopy experiments, the corresponding
13 data analysis and the stochastic modelling. S.D.T. and A.V. provided carbon/sulphur composites and
14 polysulfide powders. C.P., S.A.F. and V.W. conceptualized the work. C.P. wrote the initial version of the
15 manuscript. C.P., S.D.T., A.V., H.A., R.D, S.A.F. and V. W. contributed to results interpretation and revising
16 the manuscript.

17

18 **Competing Interests**

19 The authors declare no competing interests.

20

21

22

Supplementary Files

This is a list of supplementary files associated with this preprint. Click to download.

- [LiSSAXSSI.pdf](#)